1.3 Transmission Electron Microscopy Characterization of the Structure and Composition of the Nanofeatures in Nanostructured Ferritic Alloy MA957 — Y. Wu, E. Haney, N. Cunningham and G. R. Odette *(Univ. of California Santa Barbara)*

OBJECTIVE

The objective of this work is to characterize the number density, size distribution, structure and compositions of nanofeatures (NF) in nanostructured ferritic alloys (NFA), with emphasis on the features with diameters less than 5 nm.

SUMMARY

Bright field transmission electron microscopy (TEM), high resolution TEM (HRTEM), scanning TEM (STEM) and energy dispersive X-ray (EDX) spectroscopy were combined to comprehensively characterize the Ti-Y-O enriched nano-scale features (NF) in a nanostructured ferritic alloy (NFA), MA957. The characterization included the NF number densities, size distributions, volume fractions, crystal structures and compositions. In foil measurements were complemented by studies of NF on extraction replica foils. The conditions examined included: two heats of extruded MA957; one of these heats following long-term thermal aging at 1000°C for 19.53 kh; and two friction-stir-weld variants. The study revealed the presence of diffracting complex oxide phases that varied somewhat with the feature size. However, the smallest features, with diameters (d) < 5 nm, were found to be consistent with cubic pyrochlore $Y_2Ti_2O_7$ complex oxides with average Y/Ti ratios of ≈ 1. Long-term thermal aging coarsened the NF, while friction stir welding had relatively little effect on their number density and size distribution.

BACKGROUND

This report addresses critical issues related to the development of a potentially transformational class of materials that we call NFA that are needed for advanced nuclear fission and fusion energy systems [1]. NFA derive from roots in oxide dispersion strengthened (ODS) steels, like PM2000, that contain coarser scale oxides [2-4]. NFA manifest a combination of outstanding high temperature strength, unique thermal stability and remarkable irradiation tolerance. These outstanding characteristics derive from the presence of an ultrahigh density of Y-Ti-O rich nano-scale features (NF). The multifunctional NF impede dislocation climb and glide, enhance SIA-vacancy recombination and, perhaps most importantly, trap He in very small, high-pressure gas bubbles [2,3,5]. The bubbles reduce the amount of He reaching grain boundaries, thus avoiding severe fracture toughness loss at lower irradiation temperatures, and potential degradation of creep rupture properties at higher temperatures. In principle, He trapped in a high number density of small bubbles also mitigates many other manifestations of irradiation effects, including void swelling that is an issue at intermediate temperatures [2,3].

NFA are typically processed by ball milling elemental or pre-alloyed rapidly solidified metallic powders with yttria (Y_2O_3) powders [2-4]. Typical NFA compositions are ≈ 14Cr, 0.2Y, 0.15O, 0.4Ti, 3.0W (wt.%). Proper milling effectively dissolves the Ti, Y and O. These solutes then precipitate as NF during hot consolidation [2,6]. As expected for

precipitation processes, the NF number densities decrease with increasing consolidation temperatures. Further, Ti is needed to form NF at higher temperatures [6]. While they form rapidly, the NF are extremely thermally stable [3,7-9]. Powder consolidation is usually followed by a series of deformation processing-fabrication treatments.

While their roots were established long ago, NFA remain in the very early stages of development. One important challenge is determining the detailed characteristics of the NF, including the: number densities, size distributions, volume fractions, crystal structures and compositions. However, the detailed nature of the NF has not been clearly established. In part, this is because different characterization methods have not provided consistent results.

There are at least 6 known Y-Ti-O phases in the X-ray diffraction database, as shown in Table 1. With one exception the Y/Ti ratios of these oxides are greater than or equal to 1 and the O/(Ti+Y) ratios are greater than 1. Atom probe tomography (APT) studies have been interpreted to suggest that the NF are highly non-stoichiometric coherent transition phases [7-11], perhaps akin to G-P zones, possibly with complex core shell structures [12,13]. The APT Y/Ti ratios typically range from about 0.25 to 0.5, while the corresponding O/(Ti+Y) ratios are less than 1. Further, standard APT reconstruction algorithms indicate that the NF contains large quantities of Fe and Cr.

Table 1. Known Y-Ti-O complex oxides.

	Y-Ti-O	Crystal system	a (Å)	b (Å)	c (Å)	Reference code
1	Y_2TiO_5	orthorhombic	10.35	3.70	11.25	01-076-0787
2	Y_2TiO_5	hexagonal	3.61	3.61	11.84	00027-0981
3	$Y_2Ti_2O_7$	Cubic	10.09	10.09	10.09	01-072-0302
4	$YTiO_{2.085}$	Cubic	10.18	10.18	10.18	01-085-0001
5	$YTiO_3$	orthorhombic	5.33	5.62	7.60	01-070-2297
6	YTi_2O_6	orthorhombic	7.41	10.81	5.13	00-047-1786

In contrast, most previous TEM studies have indicated that the NF are complex oxides, primarily cubic pyrochlore $Y_2Ti_2O_7$. For example, scanning transmission electron microscopy (STEM) energy dispersive X-ray (EDX) measurements on NF extracted from NFA MA957, reported by Sakasegawa et al., indicate that the NF are non-stiochiometric $Y_2Ti_2O_7$, with Y/Ti < 1.0 for precipitates in the larger size range from up to 15 nm and Y/Ti ≈ 0.5 for the smallest pyrochlore features [14]. At largest sizes, from ≈ 15 to 35 nm, the oxides are closer to stiochiometric, with Y/Ti ≈ 1.0. Yamashita et al. also found non-stiochiometric $Y_2Ti_2O_7$, but generally with a range of Y/Ti slightly greater than 1 [15,16]. Klimiankou et al. found near stoichiometric $Y_2Ti_2O_7$ in a 9Cr NFA using electron energy loss spectroscopy (EELS), HRTEM-fast Fourier transform (FFT) power spectra indexing and energy filtered TEM (EFTEM) methods [17,18].

Early x-ray diffraction (XRD) studies by Okuda and Fujiwara also indicated the presence of $Y_2Ti_2O_7$ in a 14Cr model NFA [19]. This observation has been confirmed recently by Sasasegawa et al. based on XRD measurements on nano-pore filtered oxides extracted from a 9 Cr martensitic alloy [20]. Alinger et al. reported small angle neutron scattering (SANS) data on model NFA that were generally consistent with a mix of stoichiometric and/or non-stoichiometric oxides [5]. The SANS data also suggested that the range of

NF compositions strongly depend on the on the details of the alloy composition and processing conditions; the latter involved either hot isostatic pressing (HIPing) or powder annealing, over a range of temperatures (primarily from 850 to 1150°C) and with different time-temperature histories. Ohnuma et al. used a clever combination of SANS and small angle X-ray scattering (SAXS) to measure the composition and atom density of small NF in a 9Cr alloy, which were found to be consistent with $Y_2Ti_2O_7$ [21].

In fewer cases Y_2TiO_5 complex oxides have been reported, including one example for an NFA with lower alloy Ti contents [16], as well as in this work. Recently, Bhattacharyya et al. found a new phase in a model NFA following HIPing at 1150˚C for features in the size range from 10~50 nm [23]. HRTEM-FFT indexing showed this phase to be a probable variant of orthorhombic Y_2TiO_5, with Y/Ti ratios measured by EDX between 1 and 2. In addition, HRTEM-FFT indexing showed that small, < 5 nm $Y_2Ti_2O_7$ oxides form in NFA with the same alloy composition following HIPing at 850˚C. Studies by Ohtsuka et al. show the strong influence of the Y-Ti-O alloy composition on the structure, composition, number density and size distributions of NF [23,24]. More generally, variations in alloy compositions and processing conditions result in differences in the NF populations, suggesting that they can be manipulated to provide an optimal balance of mechanical properties and irradiation tolerance.

The previous studies described above have primarily involved characterization of larger NF with diameters (d) > 5 nm. Here we report on a detailed TEM study of a commercial vendor NFA, MA957, that extend the characterization NF to those with d < 5 nm. The MA957 was produced by INCO in the early 1980's for possible application in liquid metal breeder reactors [25]. The focus on MA957 is motivated by its role as a reference material in a wide variety of studies, using various characterization methods to examine the alloy's baseline properties and micro-nanostructures, as well as the corresponding effects of processing, joining, thermal aging and neutron or charged particle irradiations.

EXPERIMENTAL METHODS

Materials

TEM studies were carried out on 5 different MA957 conditions. Two base heats of INCO MA957 were examined in this study: a) a US heat of MA957 (US MA957) obtained from Pacific Northwest National Laboratory in the form of as extruded 25 mm diameter rods; and, b) a French heat of MA957 (FR MA957) obtained from the CEA Saclay via Oak Ridge National Laboratory. The US MA957 was also examined after: a) long term high temperature aging at 1000°C for ≈ 19.53 kh (LTTA); b) friction stir welding (FSW); and c) FSW plus annealing at 1150°C for 1 h (FSW-A). The nominal composition of MA957 is 14.9 Cr, 1.1 Ti, 0.17 Mo, 0.13 Y and 0.19 O from Y_2O_3 and ≈ 0.88 O overall, bal Fe (at.%), along with trace levels of impurity elements such as Al, Mn, Si and C. The main difference between the composition of MA957 and more recent NFA products is that the former contains Mo instead of W, and MA957 has a much higher Ti content. The base alloys were consolidated at approximately 1150°C. The FR MA957 was further processed by gun drilling and hot extrusion to form 65 mm outer diameter tubing, with a wall thickness of 9 mm. Additional processing details are not available. The LTTA of US-MA957 was carried out in a sealed tube with a He atmosphere at 1000°C. MA957 coupons were wrapped in high Cr stainless steel foil during aging to reduce the loss of this element. Approximately two millimeters of the sample was removed to avoid near

surface effects. Sectioned plates of US-MA957 with dimensions of 100 × 17 × 2 mm^3 were butt-FSW in the long dimension direction at a tool spindle speed of 130-160 rpm and travel speed of 150-200 mm/min [26]. Material from the middle of the FSW zone was characterized. The FSW material was also annealed at 1150°C for 1 h (FSW-A). The basic microstructures and properties of these alloys have been described elsewhere [27,28].

TEM

The NF were characterized both in thin TEM foils, on extraction replicas, and in one case as bulk extractions in filters. The extractions were carried out two different methods. In the first case, the polished (0.3 μm alumina finished) surface of the MA957 was electrochemically etched with a solution of 1% tetra methyl ammonium chloride-10% acetyl acetone-methanol at a potential of ≈ 6 V [15]. The etched surface was then coated with a 10-20 nm carbon film. The carbon film containing NF was subsequently removed by a second electrochemical etching step and captured on a TEM grid. This method yields both isolated and a few clustered NF on the carbon extraction replica foils. The second method was to first C-coat the polished surface (without etching) and then to remove the C film by a single electrochemical etching process. This method yielded larger coagulated clusters of small NF in some cases. The first extraction method is useful for determining the size distributions on the NF, typically using high angle annular dark field (HAADF) imaging, as well as possible NF associations with each other and with other phases. However, the extractions do not provide reliable estimates of the NF number densities (N), in part due to the complex topology of the etched surfaces. The conventionally extracted particles were also examined using HRTEM and EDX to characterize the structure and composition of the NF, respectively. The second extraction method is useful for increasing the signal for both EDX and selected area diffraction (SAD) measurements on large clusters of small NF. In the case of the FR MA957 neither extraction method produced NF that could be reliably used for EDX. In this case, the two-step extraction was carried out on somewhat roughened surfaces to produce higher areal densities of NF consistent with EDX measurements. In addition 50 nm pore size filters containing NF removed from bulk extraction solutions, that were then flash burned and fabricated into electron transparent TEM specimens, were successfully used for EDX studies of the FR MA957.

There is of course an issue concerning the effect of the extraction process on the character of the NF. We believe that this is not a significant issue for the oxides themselves since they are stable under the non-acidic etching, and the their characteristics generally resemble those observed in foil. However, this does not address the question of possible segregation of elements like Ti or O to the oxide interfaces, the termination composition of the interface or the stability of the very smallest NF even at subunit cell sizes. These important questions will be addressed in future research. What is reported here is what is observed within the limitations of the various techniques.

Thin TEM foils were prepared by either a lift-out technique using a FEI Helios-focused ion beam (FIB) tool or by twin jet electro-polishing. We focus here on the FIBed specimens, since they are far superior to electro-polished samples, mainly because of their reduced magnetic mass. The final thickness of the FIBed foils was between 30 and 70 nm. A final, low energy Ga beam (2kVand 5.5pA) was used to remove the higher

energy ion damage to achieve high quality samples. The HAADF studies were performed using an FEI TITAN at 300 kV. The in-foil studies involved conventional bright field diffraction contrast imaging and phase contrast HRTEM imaging that were performed on either an FEI TITAN at 300 kV or an FEI T20 TEM/EDX at 200 kV. EDX spectra were recorded on an FEI T20 in STEM mode with the stage tilted to 10˚, at a spot size of 3 or 4, and condenser aperture of 70 μm, which is the optimal experimental condition for measuring the composition of the small NF. Analysis of the HRTEM images was carried out by FFT power spectrum diffraction pattern indexing. The lattice spacing and inter-planar angles were measured by using Image J and Adobe Photoshop 6.0. The NF number densities were determined from the in foil micrographs. The foil thickness was measured by convergent beam electron diffraction. The size distributions of the NF were measured on both the conventional extractions and in foil specimens.

RESULTS

NF Number Densities, Size Distributions, Volume Fractions and Morphologies.

Figure 1 show examples of bright field (BF) in-foil TEM micrographs for the US (a) and French (b) MA957 NFA. Polyhedral NF are observed over a wide range of sizes and are qualitatively similar in both cases. The NF appears to be somewhat coarser in the US-M957, which also contains a higher dislocation density in this micrograph. The NF images are sharper in the FR MA957, but this is probably associated with the specific imaging conditions, rather than actual physical differences. Figure 2 shows the NF in the LTTA (1000°C for ≈ 19.53 kh) condition. While some small NF is still observed, coarsening is clearly observed after LLTA, and there is a large increase in the number of larger precipitates (> 10 nm). Figure 3 shows BF in-foil TEM images of NF in the FSW (a) and FSW-A (b).

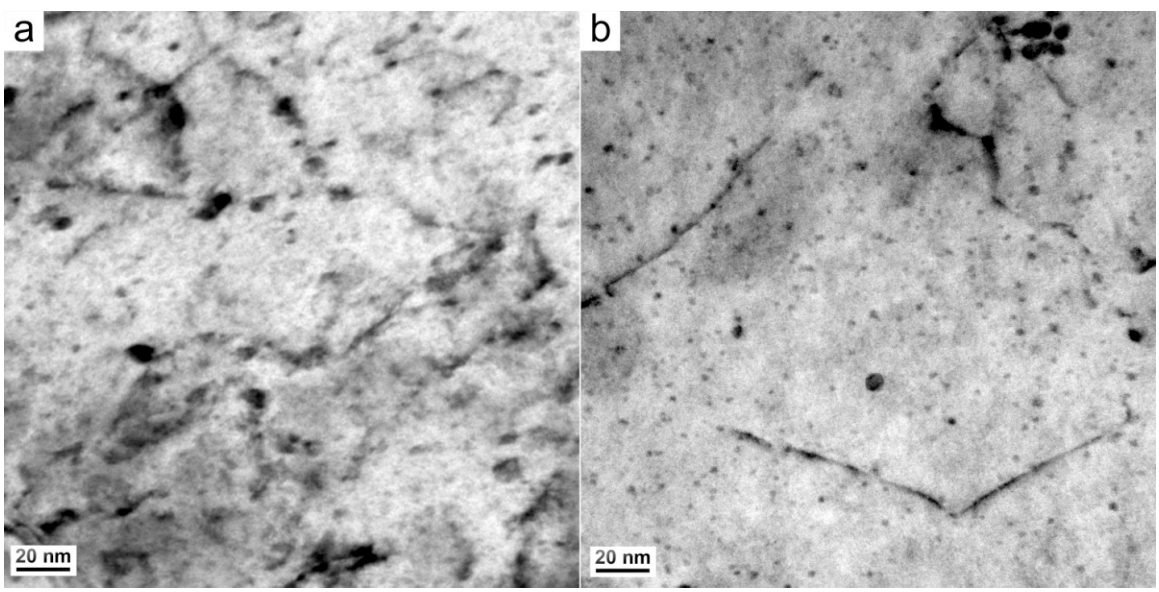

Figure 1. BF in-foil TEM images showing NF in US MA957 (a) and French MA957 (b).

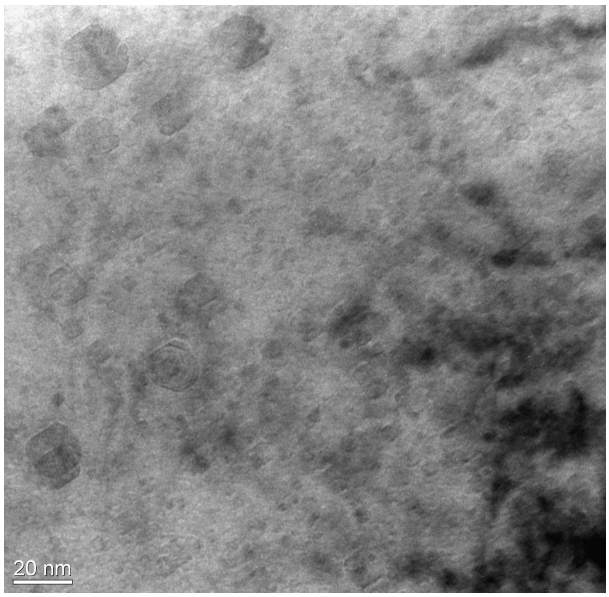

Figure 2. A BF in-foil TEM image showing NF in long-term thermal aging (LTTA) US MA957.

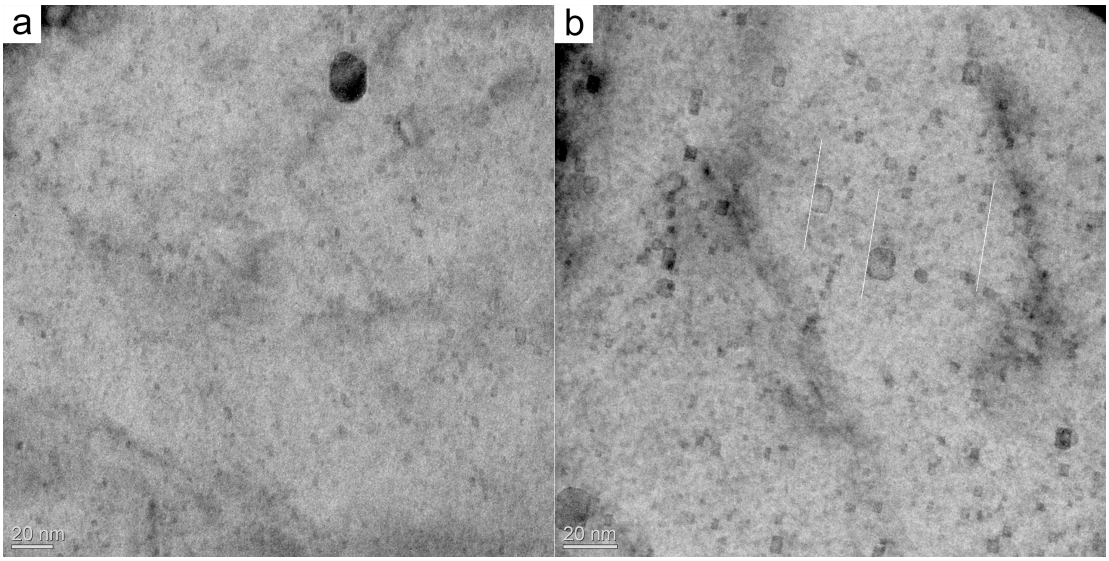

Figure 3. BF in-foil TEM images of NF in the FSW (a) and FSW-A (b) conditions.

Due to favorable imaging condition for the FSW-A sample, the NF are especially visible as truncated cubic polyhedral shapes, many with similar orientations with respect to the ferrite matrix. The NF is clearly visible down to ≈ 1 nm. The image was recorded near the <001> zone axis of the ferrite matrix, and the white dashed lines are the corresponding (100) planes. The NF number densities, N, were determined from the in-foil micrographs and are summarized in Table 2. The value of N is highest in the FR MA957 and lowest in the LTTA condition. The apparent N is nominally somewhat larger in the FSW-A condition compared to the as-extruded alloy.

Table 2. The number density and average diameter of the NF with d<10 nm in the five different MA957 conditions.

N, <d>	US MA957	French MA957	FSW	FSW-A	LTTA
N ($10^{23}/m^3$)	1.3	3.8	1.3	2.2	0.5
<d> (nm)	3.4	2.8	2.8	2.4	4.8

Figures 4 shows an example of a HAADF image of the conventional NF extractions from the FR MA957 that appear with white contrast owing to their larger average nuclear charge Z compared to the C foil. The HAADF imaging was useful in measuring the NF size distributions in the various MA957 conditions. The size distributions for the US and French-MA957 for both the in-foil and extracted NF are shown in Figure 4a and 4b. A comparison of the in foil NF size distributions for FR and US MA957 is shown in Figure 4c. In both cases, but particularly for US-MA957, the distribution is shifted to slightly larger sizes. In part this is believed to be due to agglomeration of the smaller extracted particles. The in-foil NF N = $1.3 \times 10^{23}/m^3$ and <d> = 3.4 nm for the US-MA957, versus N = $3.8 \times 10^{23}/m^3$ and <d> = 2.8 nm for the French-MA957. The corresponding average volume fractions are 0.40% and 0.61%, respectively.

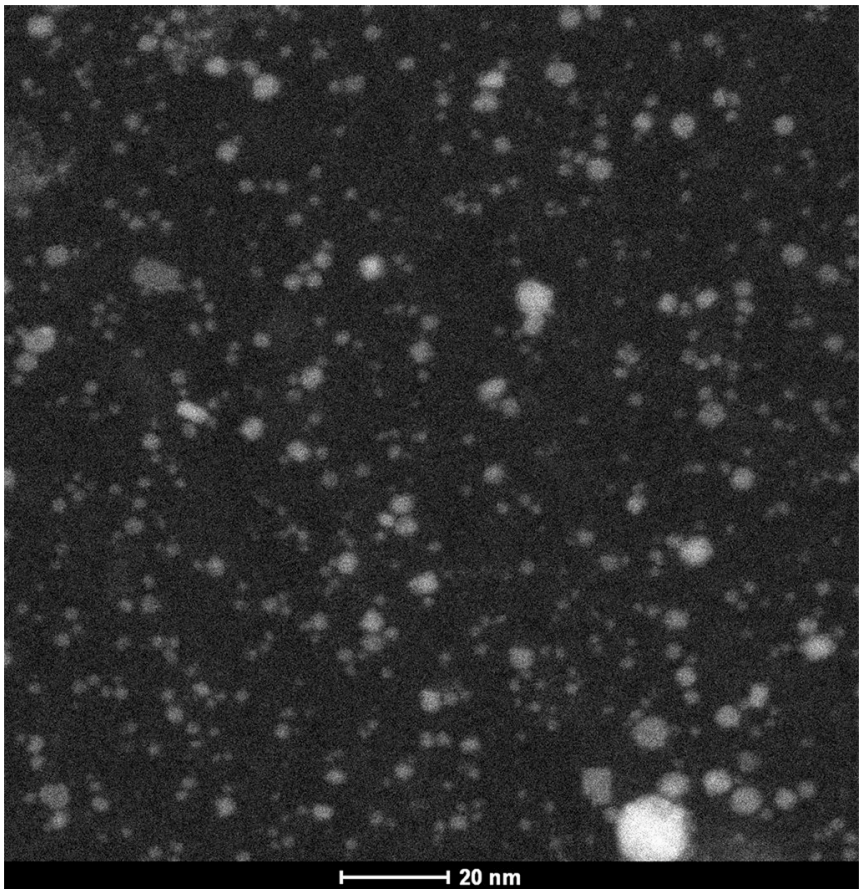

Figure 4. HAADF images of replica samples of French MA957.

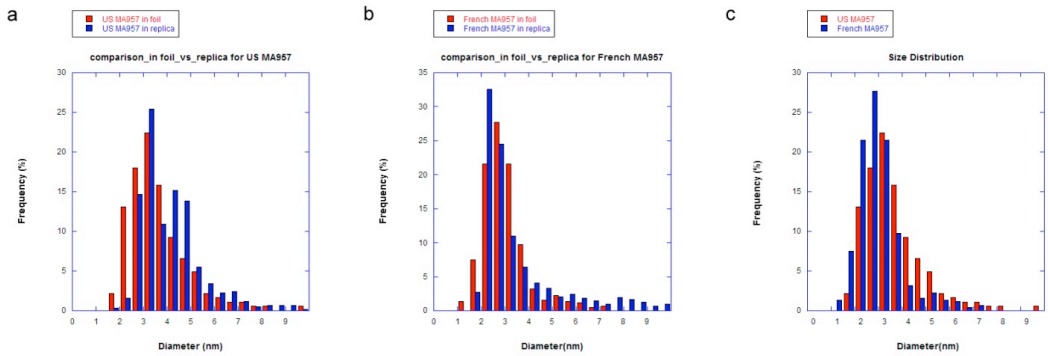

Figure 5. Comparison of in foil versus extraction replica NF size distributions in US MA957 (a) and French MA957 (b); in foil US MA957 and French MA957 NF size distributions (c).

Figure 6 shows the in-foil NF size distribution for the US-MA957 in the as extruded and LTTA condition. Significant coarsening is evident, with an increase in the average diameter from <d> = 3.4 to 4.8 nm, accompanied by a reduction in N from ≈ 1.3×10^{23} to $0.5 \times 10^{23}/m^3$. Figure 7 shows the corresponding effects of FSW (a) and FSW-A (b) on the in foil NF size distributions in US-MA957. The N and <d> for the FSW are $1.3 \times 10^{23}/m^3$ and 2.8 nm, respectively, compared to the same nominal N and slightly larger <d> = 3.4 nm in the as-extruded condition. The apparent N = $2.2 \times 10^{23}/m^3$ is larger in the FSW-A condition and the <d> = 2.4 nm is slightly smaller. This possible refinement may suggest some dissolution of the solutes during severe deformation and re-precipitation upon annealing. The small differences in NF sizes measured by TEM are consistent with independent APT and SANS data [28]. However, the latter two methods suggest reductions in N by 10% (APT) to 50% (SANS, but method this is less reliable in this case) in the FSW condition and a 50% reduction in the APT N for the US MA957 FSW-A condition.

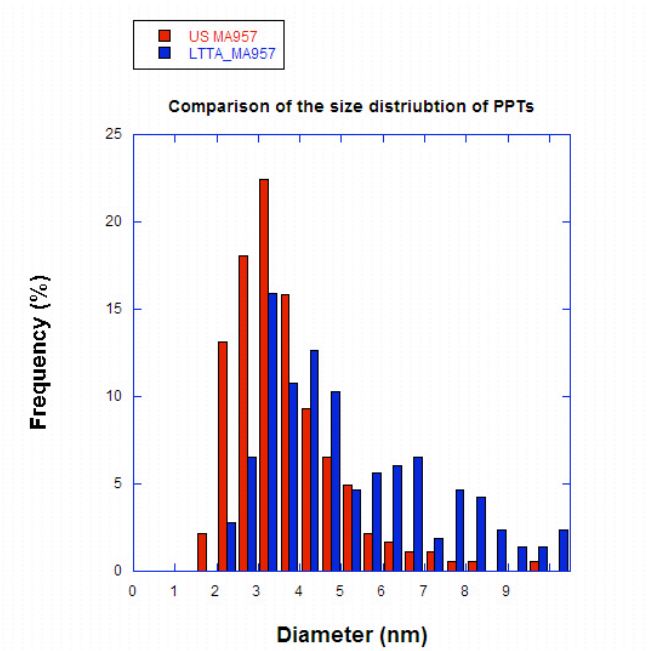

Figure 6. Comparison of the NF size distributions in the as extruded and LTTA US MA957.

It is important to put the apparent similarities and differences in the various MA957 conditions cited above in perspective. Specifically the NF populations can vary significantly over length scales of tens of nm to μm and there are limitations in all the characterization methods. Thus the most robust conclusions are that the NF are qualitatively similar in all cases, with discrete phase polyhedral morphologies from <d> ≈ 1 to > 10 nm. The NF in the US MA-957 may be slightly coarser (larger <d> and smaller N) than in the French-MA957. The NF are only moderately affected, but perhaps slightly refined and redistributed, in the FSW and FSW-A conditions. However, LTTA results in significant coarsening, as reflected in a significantly larger <d> and smaller N.

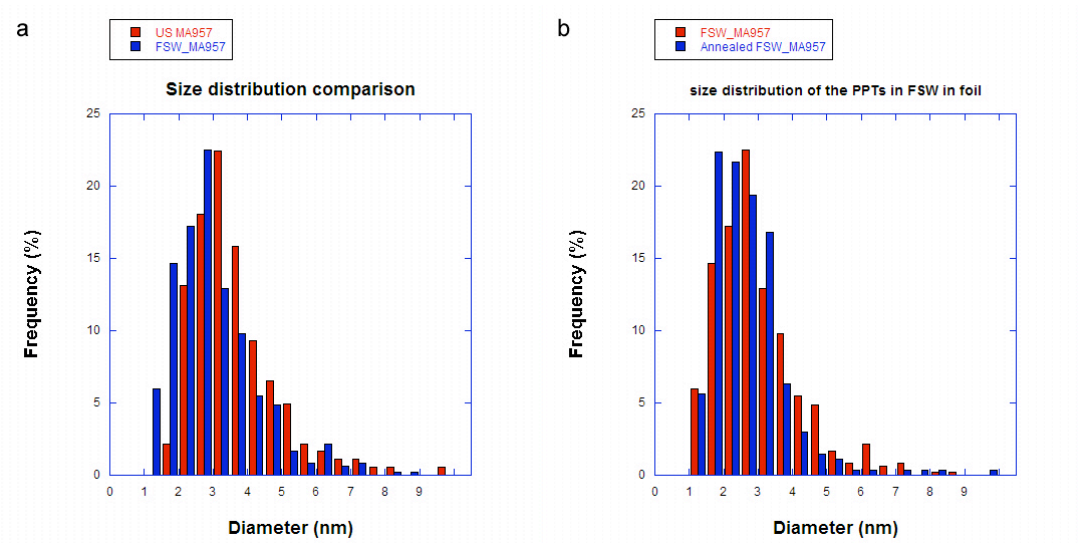

Figure 7. Comparison of the NF size distributions in the as extruded and FSW US MA957 (a); comparison of the NF size distributions in the FSW MA957 and FSW-A US MA957 (b).

The Structure and Composition of the NF in the French and US-MA957

Figure 8 shows an HRTEM image (a) of a rather large feature (d ≈ 12 nm) in the US MA957 along with the corresponding FFT power spectrum diffraction pattern (b). Table 3 shows the corresponding measured inter-planar distances and angles. These results are not consistent with either cubic $Y_2Ti_2O_7$ or hexagonal Y_2TiO_5 or YTi_2O_6. However, the diffraction data are much more consistent with orthorhombic Y_2TiO_5 <1 -15 4> or $YTiO_3$ <2 1 -2>. An even larger ≈ 20 nm feature shown in Figure 8c was not found to be consistent with any known Y-Ti oxide phase. As shown below, EDX results the features in the size range above ≈ 5 nm show Y/Ti ratios from ≈ 1.0 to 2.0. Figure 9 shows an HTREM images (a,c) and corresponding diffraction patterns (b,d) for slightly smaller ≈ 5 to 6 nm NF in the FR MA957. As shown in Table 4a the inter-planar spacing and angles are reasonably consistent with the $Y_2Ti_2O_7$ <011> (b) and <001> (d) zone axes. Similarly, a HRTEM image of a small precipitate was indexed as $Y_2Ti_2O_7$ with a <245> zone axis, as shown in Table 4b. Table 5 summarizes the results of the HRTEM FFT structure analysis of individual NF. While a large number of NF (d < 10 nm) were examined only 7 could be individually identified as possible orthorhombic Y_2TiO_5 phases in the US MA-957, and two Y_2TiO_5 plus 4 $Y_2Ti_2O_7$ NF in the FR MA957.

Figure 10 shows an example EDX spectrum for one of the smaller (d < 10 nm) extracted oxides from the US MA957, indicating that it is predominately composed of Y, Ti and O, with an average Y/Ti/O ratio of 22/16/62. Table 5 also summarizes the average Y/Ti/O compositions from EDX measurements for the US and FR MA957 for the smaller individual extracted oxides. The number of oxides measured is given in brackets in the second column. The average Y/Ti(≈ 1.4) ratio is higher in the US-MA957. The Y/Ti is lower in the French-MA957 (≈ 1.2), and is closer to stoichiometric $Y_2Ti_2O_7$. Note these compositions do not, in general, suggest that there is a mixture of $Y_2Ti_2O_7$ and Y_2TiO_5 phases, since the compositions vary from stoichiometric values for the individual oxides. In-foil EDX on the three oxides in the FSW and annealed MA957, shown in Figure 11,

with d ≈ 13.4, 9.2 and 5.2 nm, have Y/Ti ratios of 2, 0.9 and 0.8, respectively. The largest oxide is compositionally consistent with Y_2TiO_5, while the latter are more likely slightly non-stoichiometric $Y_2Ti_2O_7$.

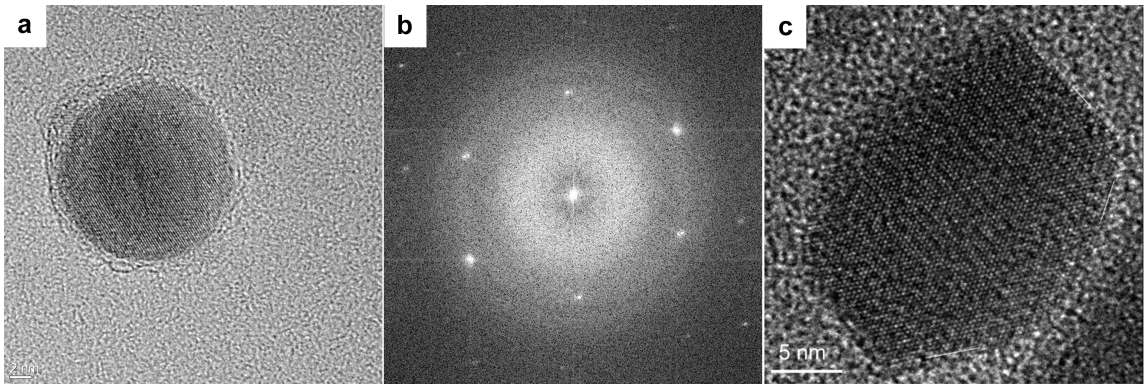

Figure 8. A HRTEM lattice image of a large feature in US MA957 (a) and the corresponding FFT power spectrum, (b) HRTEM lattice image of a large unidentified precipitate, and (c).

Table 3 measured and calculated inter-planar distances (d) and angles (a) in Fig. 8 and possible indexing.

d (Å), a	d_1	d_2	d_3	a_{12}	a_{13}	a_{23}
Measured	2.55	2.15	2.20	61.5°	66.7°	51.8°
Y_2TiO_5(o)	2.52 {401}	2.09 {313}	2.18 {1-1-4}	62.2°	67.6°	50.2°
$YTiO_3$(o)	2.50 {-120}	2.09{202}	2.18 {122}	62.3°	67.3°	50.4°

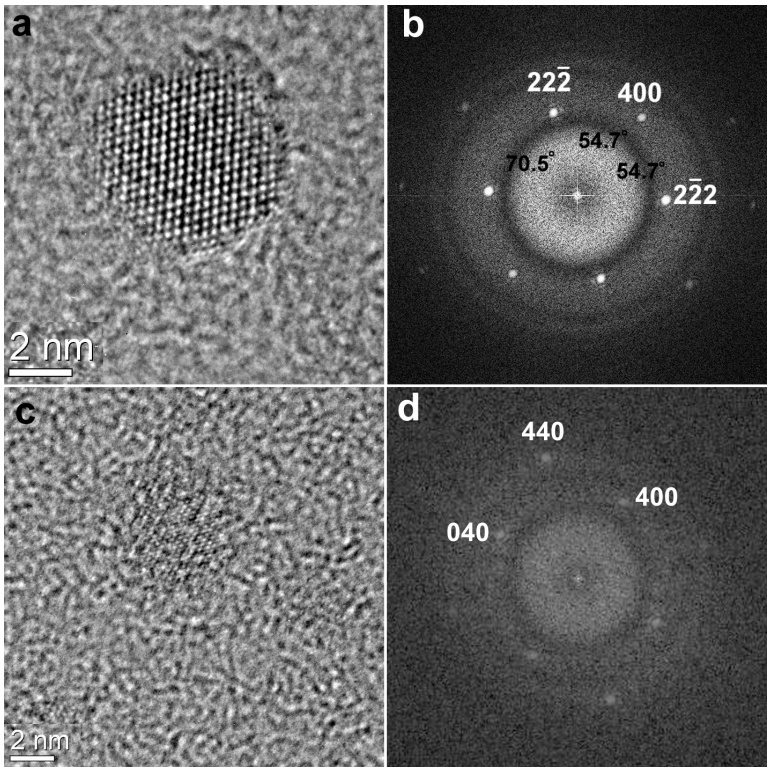

Figure 9. HRTEM lattice images of small NF in French MA957 (a, c) and the corresponding FFT power spectra (b, d).

Table 4a. Measured and calculated inter-planar distances (d) and angles (a) for Fig.9a and possible indexing.

d (Å), a	d_1{2-22}	d_2{400}	d_3{22-2}	a_{12}	a_{23}	a_{31}
Measured	2.96	2.60	3.09	53.4°	55.6°	71.0°
$Y_2Ti_2O_7$	2.90	2.52	2.90	54.7°	54.7°	70.5°

Table 4b. Measured and calculated inter-planar distances (d) and angles (a) for Fig.9c and possible indexing.

d (Å), a	d_1{400}	d_2{440}	d_3{040}	a_{12}	a_{13}
measured	2.52	1.78	2.52	45.15°	90°
$Y_2Ti_2O_7$	2.65	1.87	2.65	45°	90°

Table 5. Summary of HRTEM and EDX results from individual NF (d < 10 nm).

MA957	<Y/Ti/O (#)	Phase				
		Unknown	Not Indexed	Pos. Y_2TiO_5	Pos. $Y_2Ti_2O_7$*	Pos. $Y_2Ti_2O_7$
FR	23/19/58 (27)	4	17	0	1	4
US	21/15/64 (12)	3	61	2	5	6

* Only one set of planes

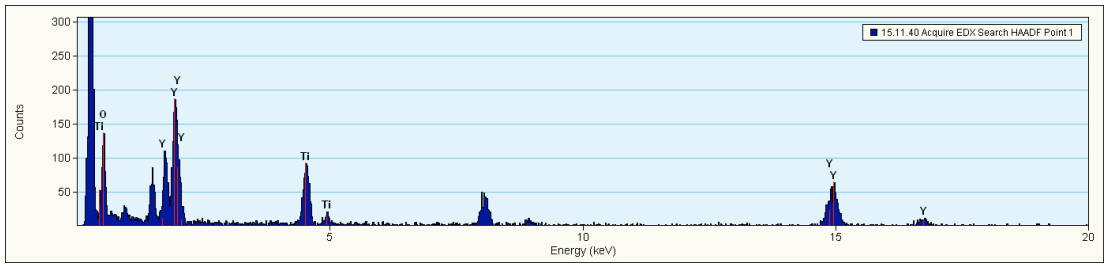

Figure 10. An example of an EDX spectrum for a small (d ≈ 10 nm) NF.

HRTEM and EDX characterization of the structure of individual NF in the range of d < 5 nm is more difficult. Thus we have used the second replica extraction procedure to produce higher local densities or aggregated clusters of NF that were characterized by HRTEM, selected area diffraction (SAD) and EDX. Figure 12a shows an example of high local densities of polyhedral NF extracted from US MA957. Figure 12b shows a SAD pattern taken for the group of small particles. In this case the SAD has been calibrated to a GaN standard shown in Figure 12c. Table 6 shows that the SAD rings indicate NF d-spacings that are highly consistent with $Y_2Ti_2O_7$. HRTEM FFT power spectra on groups of these oxides yield similar results.

Table 6. Summary of d spacing's measured from the SAD ring pattern shown in Fig. 12(b).

Compound	hkl	Measured	Calculated
GaN Standard	100	2.763	2.763
$Y_2Ti_2O_7$	222	2.926	2.91
$Y_2Ti_2O_7$	400	2.563	2.52
$Y_2Ti_2O_7$	440	1.798	1.78
$Y_2Ti_2O_7$	622	1.540	1.52

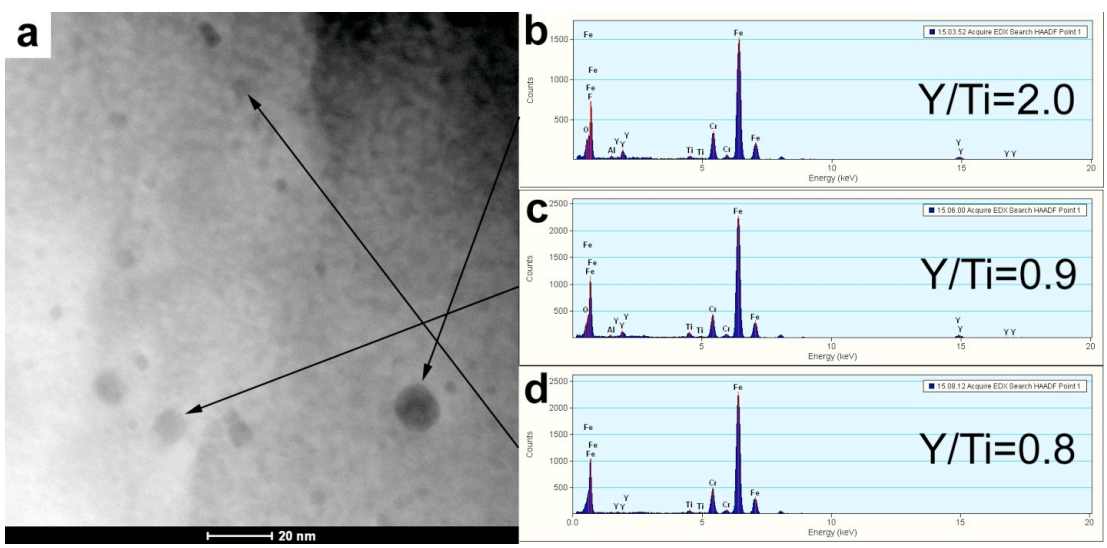

Figure 11. A HAADF image of FSW-A US MA957 (a) and corresponding EDX on the three indicated NF (b, c, d).

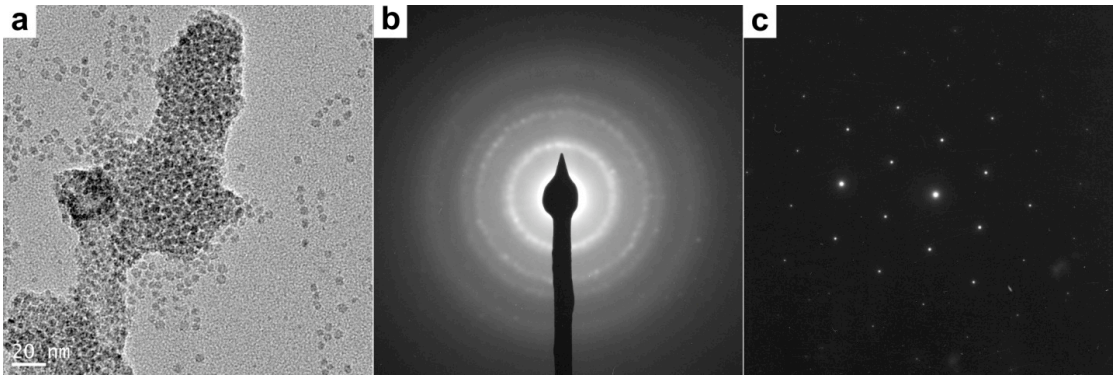

Figure 12. An example of high local densities of polyhedral NF extracted from US MA957 by the second replica method (a); a SAD pattern taken for the clump of particles (b); the SAD has been calibrated to a GaN standard (c).

Figure 13a shows a cluster of oxides and Figure 13b the corresponding EDX measurements. The aggregate compositions are 15.5% Y (L), 15.4% Ti (K), 1.1% Cr (K) and 68% O (K). These values are very close to the composition of $Y_2Ti_2O_7$ 18.2% Y, 18.2% Ti and 63.6% O. EDX of the small precipitates in the FR MA957 were carried out on both rough surface two-step extractions and the filtered bulk extractions. The EDX Y/Ti ratio also averages ≈ 1 in these cases.

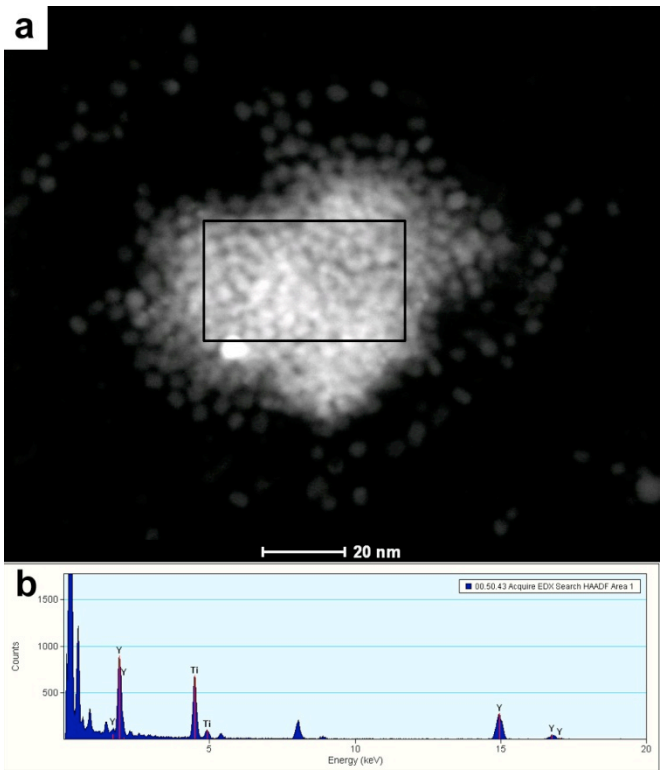

Figure 13. A HAADF image of a cluster of small NF (a); andm the corresponding EDX spectrum (b).

DISCUSSION, SUMMARY AND CONCLUSIONS

The sizes (d) and number densities (N) of the NF appear to be generally similar in the FR and US MA957 heats. TEM indicates that the FSW and FSW-A conditions are also similar to one another and to the parent as extruded US MA957. However, it is noted that the in foil estimates of the N for US-MA957 found here are somewhat lower than previously reported [28]. Further, SANS and APT data suggest that there is a more significant decrease in N in the FSW and, especially, the FSW-A conditions than indicated by the current TEM data. LTTA at 1000°C for 19.53 kh coarsens the NF with a significant increase in <d> and decrease in N, consistent with trends observed in APT and SANS studies [29].

The HRTEM-FFT, SAD and EDX data indicate that the smallest (d < 5 nm) NF in MA957 are cubic pyrochlore $Y_2Ti_2O_7$ complex oxides, broadly consistent with most previous TEM and XRD observations of larger precipitates in similar alloys. BF TEM suggests that the NF have an orientation relationship (OR) with the (100) planes in the Fe-Cr ferrite matrix. Work is continuing to establish the full OR, including the corresponding oxide interface planes and directions.

Notably, the TEM results are inconsistent with interpretation of AP data that suggest that the NF are far from equilibrium, perhaps coherent, transition phase solute clusters with much lower Y/Ti and O/(Ti + Y) ratios as well as very high Fe and Cr contents even in the center of small NF. Thus, we believe that the conclusion regarding their being an APT Fe-Cr content artifact is robust. However, the observations reported here do not address the possibility that solutes segregated to the NF interfaces, perhaps forming a $Y_2Ti_2O_7$ oxide and a Ti and O enriched shell.

REFERENCES

1. S. J. Zinkle and J. T. Busby, *Mater. Today* **12**, 12-11 (2009).
2. G. R. Odette, M. J. Alinger, and B. D. Wirth, *Annu. Rev. Mater. Res.* **38**, 471 (2008).
3. G. R. Odette and D. T. Hoelzer, *JOM* **62**, 84 (2010).
4. G. R. Odette, P. Miao, D. J. Edwards et al., "Helium Transport, Fate and Management in Nanostructured Ferritic Alloys: In Situ Helium Implanter Studies," *J. Nucl. Mater.* (2010) in press.
5. M. J. Alinger, G. R. Odette and D. T. Hoelzer, *Acta Mater.* **57**, 392 (2009).
6. N. J. Cunningham, G. R. Odette and E. Stergar, Fusion Materials Semiannual Progress Report for the Period Ending December 31, 2010, DOE-ER-0313/49 (2011) 1.
7. M. K. Miller, D. T. Hoelzer, E. A. Kenik, and K. F. Russell. *J. Nucl. Mater.* **329**, 338 (2004).
8. M. K. Miller, D. T. Hoelzer, E. A. Kenik, and K. F. Russell, *Intermetallics* **387**, 133–134 (2005).
9. M. K. Miller, K. F. Russell, and D. T. Hoelzer, *J. Nucl. Mater.* **351**, 261 (2006).
10. M. K. Miller, E. A. Kenik, K. F. Russell, L. Heatherly, D. T. Hoelzer, and P. J. Maziasz, *Mater. Sci. Eng. A* **353**, 140 (2003).
11. P. Pareige, M. K. Miller, R. E. Stoller, D. T. Hoelzer, E. Cadel, and B. Radiquet, *J. Nucl. Mater.* **360**, 136-43 (2007).
12. E. A. Marquis, *Appl. Phys. Lett.* **93**, 181904 (2008).

13. C. A. Williams, E. A. Marquis, A. Cerezo and G. D. W. Smith, *J. Nucl. Mater.* **400**, 37 (2010).
14. H. Sakasegawa, L. Chaffron, F. Legendre, L. Boulanger, T. Cozzika, M. Brocq, and Y. de Carlan, *J. Nucl. Mater.* **384**, 115 (2009).
15. S. Yamashita, S. Ohtsuka, N. Akasaka, S. Ukai, and S. Ohnuki, Phil. Mag. Lett, **84**, 525 (2004).
16. S. Yamashita, N. Akasaka, and S. Ohnuki, *J. Nucl. Mater.* **329**, 377 (2004).
17. M. Klimiankou, R. Lindau, and A. Möslang, *J. Nucl. Mater.* **329**, 347 (2004).
18. M. Klimiankou, R. Lindau, and A. Möslang, *Micron*, **36**, 1 (2005).
19. T. Okuda and M. Fujiwara, *J. Mater. Sci. Letts.* **14**, 1600 (1995).
20. H. Sakasegawa, M. Tamura, S. Ohtsuka, S. Ukai, H. Tanigawa, A. Kohyama, M. Fujiwara, J. Alloys and Compounds **452**, 2 (2008).
21. M. Ohnuma, J. Suzuki, S. Ohtsuka, S.-W. Kim, T. Kaito, M. Inoue, H. Kitazawa, Acta Materialia **57**, 5571 (2009).
22. D. Bhattacharyya, P. Dickerson, G. R. Odette, S. A. Maloy, A. Misra, and M. A. Nastasi, this report.
23. S. Ohtsuka, S. Ukai, M. Fujiwara, T. Kaito, and T. Narita, *J. Nucl. Mater.* **329**, 372 (2004).
24. S. Ohtsuka, S. Ukai, M. Fujiwara, T. Kaito, and T. Narita, *J. Phys. Chem. of Solids* **66**, 571 (2005).
25. J. J. Fisher, "Dispersion Strengthened Ferritic Alloy for Use in Liquid-Metal Fast Breeder Reactors," U.S. Patent No. 4,075,010 (1978).
26. J. Bernath and J. Gould, Report on Development of Candidate Joining Technology for MA957 Sheet, Edison Welding Institute, Columbus, OH, USA, March 2005.
27. P. Miao, G. R. Odette, T. Yamamoto, M. Alinger, and D. Klingensmith, *J. Nucl. Mater.* **377**, 59 (2008).
28. A. Etienne, N. J. Cunningham, Y. Wu and G. R. Odette, Mater. Sci. and Tech. 724, 27-4 (2011).